Chemical Trends in the Lattice Thermal Conductivity of Li(Ni, Mn, Co)O_2 (NMC) Battery Cathodes

Hui Yang,[†,#] Christopher N. Savory,[‡,#] Benjamin J. Morgan,[¶,#] David O. Scanlon,[‡,§,#] Jonathan M. Skelton,[*,‖] and Aron Walsh[*,†,⊥,#]

†*Department of Materials, Imperial College London, Exhibition Road, London SW7 2AZ, UK*

‡*University College London, Department of Chemistry and Thomas Young Centre, 20 Gordon Street, London WC1H 0AJ, UK*

¶*Department of Chemistry, University of Bath, Claverton Down, Bath BA2 7AY, UK*

§*Diamond Light Source Ltd., Diamond House, Harwell Science and Innovation Campus, Didcot, Oxfordshire OX11 0DE, UK*

‖*School of Chemistry, University of Manchester, Oxford Road, Manchester M13 9PL, UK*

⊥*Department of Materials Science and Engineering, Yonsei University, Seoul 03722, Korea*

#*The Faraday Institution, Quad One, Harwell Science and Innovation Campus, Didcot, UK*

E-mail: jonathan.skelton@manchester.ac.uk; a.walsh@imperial.ac.uk

Abstract

While the transport of ions and electrons in conventional Li-ion battery cathode materials is well understood, our knowledge of the phonon (heat) transport is still in its infancy. We present a first-principles theoretical investigation of the chemical trends in the phonon frequency dispersion, mode lifetimes, and thermal conductivity in the series of layered lithium transition-metal oxides $Li(Ni_xMn_yCo_z)O_2$ ($x+y+z=1$). The oxidation and spin states of the transition metal cations are found to strongly influence the structural dynamics. Calculations of the thermal conductivity show that $LiCoO_2$ has highest average conductivity of $45.9\,W\,m^{-1}\,K^{-1}$ at $T = 300$ K and the largest anisotropy, followed by $LiMnO_2$ with $8.9\,W\,m^{-1}\,K^{-1}$, and $LiNiO_2$ with $6.0\,W\,m^{-1}\,K^{-1}$. The much lower thermal conductivity of $LiMnO_2$ and $LiNiO_2$ is found to be due to 1–2 orders of magnitude shorter phonon lifetimes. We further model the properties of binary and ternary transition metal combinations to examine the possible effects of mixing on the thermal transport. These results serve as a guide to ongoing work on the design of multi-component battery electrodes with more effective thermal management.

Introduction

The lithium nickel-manganese-cobalt oxide (NMC) alloys $Li(Ni_xMn_yCo_z)O_2$ ($x + y + z = 1$ and x, y, and z are molar fractions) are among the most widely used cathode materials in Li-ion batteries (LIBs).[1,2] NMC alloys are formed by partially replacing the transition metal in the $LiCoO_2$ with Ni and/or Mn, which preserves the favourable voltage characteristics but provides a higher capacity of up to $200\,mA\,h\,g^{-1}$, while also addressing cost and abundance issues.[3,4] The alloying also helps to enhance the discharge capacity[5,6] and to provide better cycle life and thermal stability,[7,8] together with improved rate capability.[5]

Optimizing NMC compositions has focused mainly on the specific energy, power, and cycle life,[9,10] as well as the ionic and electronic transport,[11] with relatively little attention devoted to thermal management.[12] However, the thermal conductivity of battery electrodes

is an important factor in capacity fade, power fade, thermal runaway, shelf discharge, and other performance and safety issues that are critical considerations for high-performance LIBs.[12] The thermal conductivities of battery components are also important parameters in modelling studies aiming to optimise battery design, for example, by improving surface and tab cooling.[13,14]

There is a relatively small body of literature on thermal transport in NMC electrode materials, with reported values ranging from $0.14 - 40\,\mathrm{W\,m^{-1}\,K^{-1}}$.[15–18] There has not yet however been a systematic study of the NMC system, nor of the expected anisotropy in the thermal transport of the layered materials used in LIB electrodes.[19] This is due mainly to the difficulties inherent in preparing high-quality samples for experimental measurements and to the complexity of modelling heat transport using first-principles calculations.[12,15] In a recent theoretical study, we used the single-mode relaxation-time approximation to study the heat transport in pristine $LiCoO_2$.[19] Our results showed good agreement with available experimental data and highlighted substantial differences between the in-plane and cross-plane thermal transport, which has important implications for thermal management in LIBs.

In this work, we report a systematic exploration of the thermal transport in the $LiNiO_2$, $LiMnO_2$ and $LiCoO_2$ endpoints of the NMC system, and we further investigate solid solutions by considering the enhancement of phonon scattering due to mass variation at the transition metal sites. Our results show that the three $LiMO_2$ (M = Co, Ni, Mn) endpoints have fundamentally different vibrational and thermal properties, and that optimizing the ratio of the transition metals in the NMC alloys allows the the thermal conductivity to be systematically tuned. This work thus provides important direction and reference data for the design of future electrode materials for safer, higher-performance batteries.

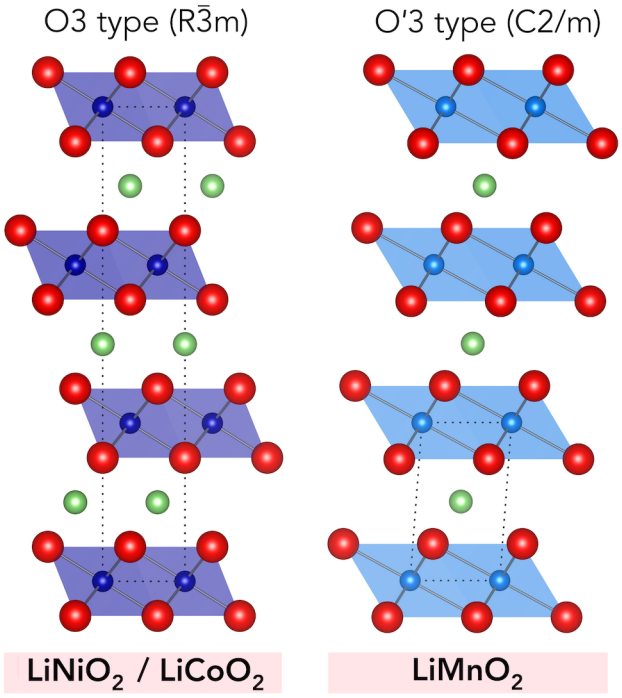

Figure 1: Crystal structures of the $LiMO_2$ (M = Ni, Co, Mn) endpoints in the NMC oxide system. $LiNiO_2$ and $LiMnO_2$ adopt an O3-type layered structure, which is shown along the $\langle 100 \rangle$ direction in the hexagonal setting. $LiMnO_2$ adopts an O'3-type layered structure, which allows for stronger octahedral distortions, and is shown along the $\langle 100 \rangle$ direction in the primitive unit cell. The Li and O ions are shown as green and red spheres, respectively, and the MO_6 octahedra are shown as shaded polyhedra. The images were generated using VESTA.[20]

Methods

First-principles electronic-structure calculations

The starting points for our calculations were the experimentally-determined structures of $LiCoO_2$,[21] $LiNiO_2$,[22] and $LiMnO_2$[23] shown in Figure 1. We use the same methodology as in our previous study on $LiCoO_2$, for which the computational details can be found in Ref.[19] Calculations were performed using the plane-wave pesudopotential density-functional theory (DFT) formalism as implemented in `VASP`.[24,25] The HSE06 hybrid functional[26] was used alongside the Tkatchenko-Scheffler dispersion correction[27] with iterative Hirshfeld partitioning[28] and PBE0 damping ($S_r = 1.287$) for both geometry optimization and single-point calculations to obtain the second- and third-order interatomic force constants (IFCs). Γ-centered Monkhorst-Pack k-point meshes with $6 \times 6 \times 6$ subdivisions were used for $LiNiO_2$ and $LiCoO_2$, while a $9 \times 8 \times 5$ mesh was used for $LiMnO_2$ due to its anisotropic unit cell.[29] The energy cutoff for the plane-wave basis set was set to 600 eV, and projector augmented-wave pseudopotentials[30] were used to model the ion cores with the following valence electron configurations: Li – $1s^2 2s^1$, Mn – $3p^6 4s^2 3d^5$, Co – $4s^2 3d^7$, Ni – $4s^2 3d^8$, and O – $2s^2 2p^4$. For Co and Ni, the pesudopotentials include the 4s and 3d electrons, while the Mn potential also includes the semi-core 3p electrons; this is due these states being higher in energy in the earlier transition metals and thus closer to the valence states. All calculations were spin-polarised with low-spin Co(III) (d^6, $S = 0$), high-spin Mn(III) (d^4, $S = 2$), and low-spin Ni(III) (d^7, $S = 1/2$).

Lattice-dynamics calculations

Harmonic lattice-dynamics calculations were set-up and post-processed using `Phonopy`.[31] The thermal conductivity (κ) was obtained by computing the third-order IFCs and solving the phonon Boltzmann transport equations within the single-mode relaxation-time approximation using `Phono3py`.[32] As described below, the reported structures of $LiCoO_2$ and $LiNiO_2$

were found to be dynamically stable with no imaginary branches in the harmonic phonon dispersion, while the dispersion of $LiMnO_2$ displayed a prominent imaginary mode at the $q_M = (0, \frac{1}{2}, \frac{1}{2})$ wavevector. This necessitated a $1 \times 2 \times 2$ supercell expansion to represent the distorted energy minimum. For $LiCoO_2$ and $LiNiO_2$ the second- and third-order IFCs were computed in $3 \times 3 \times 3$ and $2 \times 2 \times 2$ supercells, respectively, containing 108 and 32 atoms. For the expanded $LiMnO_2$ structure obtained after removing the soft mode, the second- and third-order IFCs were computed in $4 \times 2 \times 1$ and $3 \times 1 \times 1$ supercells, respectively, containing 128 and 48 atoms. The second-order IFCs were computed using a finite-displacement step size of 10^{-2} Å, and the third-order IFCs were calculated with step sizes of 3×10^{-2} Å for $LiCoO_2$ and $LiMnO_2$ and 2×10^{-2} Å for $LiNiO_2$. The smaller step size for $LiNiO_2$ was found to be necessary to reduce the numerical noise in the third-order IFCs (see Supporting Information). During the thermal-conductivity calculations, the additional phonon scattering introduced by mass variation at the atomic sites was modeled by including an additional isotope-scattering term in the calculation of the phonon linewidths, as outlined in Ref.[33]

Results and discussion

Crystal structures

The layered crystal structures of the $LiMO_2$ family are illustrated in Figure 1 and the optimised structural parameters are listed in Table 1. Following geometry optimisation, $LiCoO_2$ retains rhombohedral symmetry with space group $R\bar{3}m$. For $LiNiO_2$ and $LiMnO_2$, substantial Jahn-Teller (JT) distortions emerge during the crystal structure optimisation, which are more pronounced in the latter. Similar observations were made by Du *et al.*[34]

To compare the coordination environments we employ the distortion index of Baur[35] to describe the distribution of oxide ions around the transition metal centres with bond lengths

l_i:

$$JT = \frac{1}{n}\sum_{i=1}^{n}\frac{|l_i - l_{av}|}{l_{av}} \quad (1)$$

The analysis yields a value of zero for LCO, 0.04 for LNO, and 0.09 for LMO. For low-spin octahedral Co(III) (d^6), the three t_{2g} orbitals are fully occupied and there is no driving force for a JT distortion. Octahedral Mn(III) (d^4) and Ni(III) (d^7) possess partially-occupied t_{2g} and e_g orbitals, respectively, and therefore JT distortions to lift the degeneracy are expected.

Table 1: Optimized crystal structure parameters for $LiCoO_2$, $LiNiO_2$ and $LiMnO_2$ (DFT/HSE06). Values are shown for the primitive unit cells. Two entries are given for $LiMnO_2$ - the δ phase refers to the lower-symmetry structure obtained after condensing the soft phonon mode.

	a	b	c	α	β	γ	d(M-O) Å	JT[a]	spacegroup
$LiCoO_2$	4.912	4.912	4.912	32.984	32.984	32.984	1.90	0.00	$R\bar{3}m$
$LiNiO_2$	4.899	5.004	5.001	33.751	32.925	32.935	1.84, 1.92, 2.08	0.04	$C2/m$
$LiMnO_2$	3.049	3.049	5.320	113.09	113.09	54.66	1.91, 2.30	0.09	$C2/m$
$LiMnO_2$ (δ)	5.320	2.799	5.417	90.000	116.20	90.000	1.91, 1.92, 2.31	0.09	$P2_1/c$

[a]Jahn-Teller distortion index as defined in Equation 1.

Harmonic phonons

The harmonic phonon dispersion for each of the three endmembers is shown in Figure 2. The four atoms in the primitive unit cells result in $3N = 12$ phonon modes in all three systems. $LiCoO_2$ and $LiNiO_2$ have similar phonon dispersion, and the real frequencies across the vibrational Brillouin zone confirm both to be dynamically stable structures.

The atom-projected partial density of states (PDOS) are shown to the right of the dispersion in Figure 2. Across the three structures the medium and low frequency modes are mainly due to motion of Li and the transition-metals, while the high frequency modes above 14 THz are vibrations involving the transition metal and O atoms. The lower vibrational frequencies of the latter modes in $LiNiO_2$ and $LiMnO_2$ are due to the weaker bonding interaction between the metals and the oxygen atoms with the partially-elongated Mn-O and

Ni-O bonds due to the JT distortions.

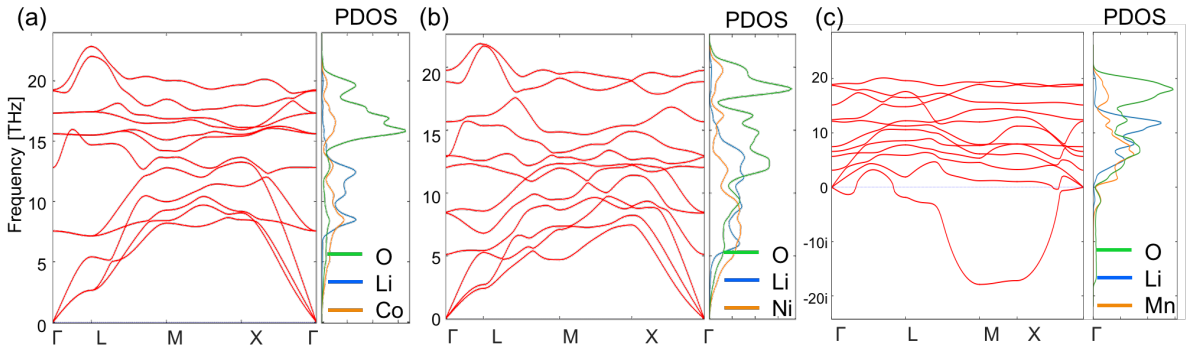

Figure 2: Harmonic phonon dispersion and atom-projected density of states (PDOS) of $LiCoO_2$, $LiNiO_2$ and $LiMnO_2$.

One of the three acoustic modes softens on going from LCO to LNO, and becomes imaginary at the M wavevector in LMO ($q_M = (0, \frac{1}{2}, \frac{1}{2})$). The presence of imaginary harmonic modes indicates a dynamical instability, i.e. that the LMO structure is a local energy maximum on the structural potential-energy surface. The M wavevector indicates that a $1 \times 2 \times 2$ supercell expansion of the $LiMnO_2$ primitive cell, i.e. a fourfold increase in volume from 4 to 16 atoms, is required to accommodate a full distortion period. We therefore generated a supercell and displaced the atoms along the imaginary mode to locate the minimum before performing a final geometry optimisation. The transformation leads to a strong JT distortion of the MnO_6 octahedra, which results in three distinct bond lengths (Figure 3a), lowers the symmetry from $C2/m$ to $P2_1/c$, and lowers the energy by 1.7 meV per formula unit. As shown in Figure 3b, the structure has a more complex dispersion, with 48 bands at each wavevector, but no imaginary modes, indicating it to be an energy minimum.

Lattice thermal conductivity

Each phonon mode λ makes a contribution κ_λ to the macroscopic lattice thermal conductivity κ. κ_λ are the product of the modal heat capacities C_λ, group velocities ν_λ, and phonon mean free paths $\nu_\lambda \times \tau_\lambda$, where τ_λ are the phonon lifetimes. The macroscopic κ is obtained by

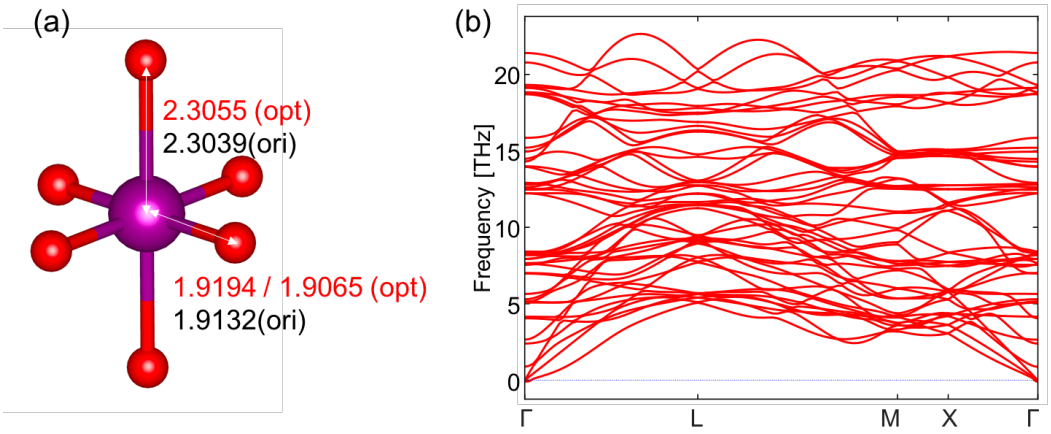

Figure 3: (a) Distortion of the MnO_6 octahedra in the optimised $LiMnO_2$ structure (bond lengths in Å). (b) Phonon dispersion of the expanded $LiMnO_2$ structure obtained after mode following and geometry optimisation to condense the imaginary mode.

summing over all the modes on a grid of wavevectors q sampling the phonon Brillouin zone and normalising for the cell volume V and the number of wavevectors N included in the summation.

$$\kappa = \frac{1}{NV} \sum_{\lambda} C_\lambda \nu_\lambda \otimes \nu_\lambda \tau_\lambda \tag{2}$$

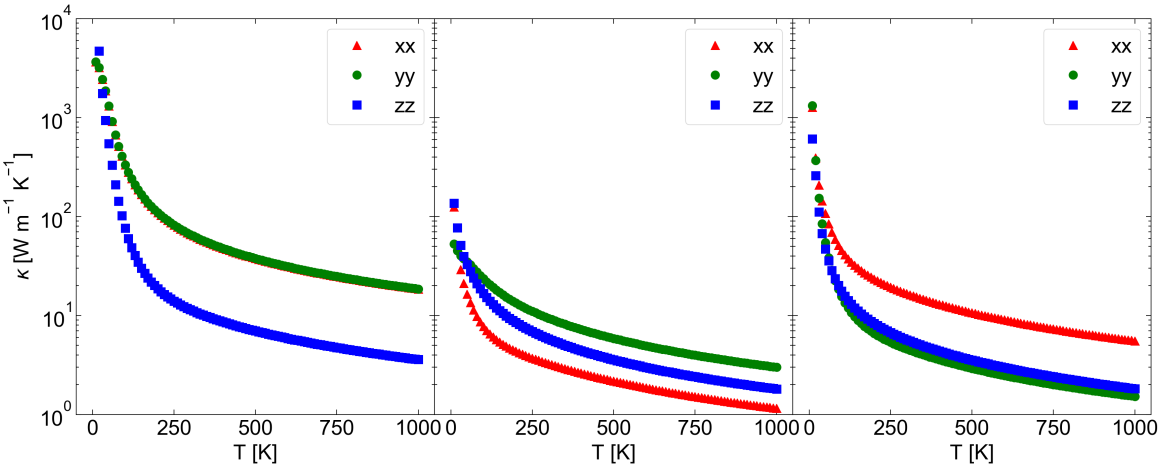

Figure 4: Thermal conductivity κ as a function of temperature for (left) $LiCoO_2$, (centre) $LiNiO_2$ and (right) $LiMnO_2$. Each plot shows the conductivity separately along the principal xx, yy and zz directions.

The thermal conductivity of the three oxides are plotted in Figure 4. These values likely

represent an upper limit, as they only account for three-phonon scattering processes and do not include additional scattering from higher-order scattering processes, natural isotope effects, defects, grain boundaries, *etc.* that generally reduce the heat conduction.[15–18]

We note that force-constant symmetrisation was found to have a large effect on the calculated thermal conductivities. Both the second- and third-order IFCs are computed using finite differences, which unavoidably results in a small amount of numerical noise. This is particularly true for the third-order IFCs, which are double derivatives of the forces with respect to atomic displacements. Symmetrisation ensures that the phonon frequencies obey the acoustic-sum rule, and that the second- and third-order IFCs are consistent with the underlying crystal symmetry, and is typically a default option in first-principles lattice-dynamics codes. Symmetrisation increases the average thermal conductivity $\kappa_{\text{ave}} = \frac{1}{3}(\kappa_{xx} + \kappa_{yy} + \kappa_{zz})$ at 300 K by 25 % and 20 % for $LiCoO_2$ and $LiMnO_2$, respectively, while it increases κ_{ave} by nearly a factor of three for $LiNiO_2$ The averaged value of $47.8\,\text{W}\,\text{m}^{-1}\,\text{K}^{-1}$ obtained for $LiCoO_2$ is thus higher than our previously-calculated value of $38.5\,\text{W}\,\text{m}^{-1}\,\text{K}^{-1}$, where we did not impose symmetry on the calculated IFCs. We also carefully checked the convergence of the calculated thermal conductivity with respect to the lifetime-sampling mesh and interaction range (supercell size) used to compute the third-order IFCs, and in particular noted that 3rd-order interactions in $LiNiO_2$ appear to extend beyond the first coordination shell (containing the six nearest neighbours). Detailed discussion can be found in the Supporting Information.

The thermal conductivity decays exponentially with increasing temperature, due to the larger thermal population of phonon modes, leading to enhanced phonon scattering. Table 2 lists the room-temperature (300 K) thermal conductivity along each crystallographic direction together with the isotropic average, with and without scattering due to natural isotopic mass variation. The thermal conductivity of $LiCoO_2$ is $66.0\,\text{W}\,\text{m}^{-1}\,\text{K}^{-1}$ in the hexagonal ab plane and > 80 % smaller along the out-of-plane c direction. The averaged thermal conductivity of $LiMnO_2$ ($9\,\text{W}\,\text{m}^{-1}\,\text{K}^{-1}$) is $\sim$20 % of that in $LiCoO_2$ and is much less anisotropic.

$LiNiO_2$ has the lowest average thermal conductivity of $6.2\,W\,m^{-1}\,K^{-1}$, which is almost 8 $\times$ smaller than $LiCoO_2$. The JT distortions in the $LiMnO_2$ and $LiNiO_2$ structures result in different easy/hard axes for transport in these systems compared to $LiCoO_2$. Including isotope effects reduces the average thermal conductivities by 1–4 % and has the largest effect on $LiCoO_2$.

We also calculated the thermal conductivity at a smaller set of temperatures by direct solution of the full linearized Boltzmann transport equation (LBTE). This method improves upon the single-mode relaxation-time approximation (RTA) by taking into account heat transport through collective phonon modes, but incurs a substantial additional overhead due to the need to form and diagonalize a large collision matrix at each calculation temperature. We find that the LBTE method predicts 16, 20 and 6 % increases in the 300 K κ_{ave} of $LiCoO_2$, $LiNiO_2$ and $LiMnO_2$, respectively, indicating that collective phonons may play a significant role in the thermal transport in these materials.

Feng *et al.* predicted the thermal conductivity of $LiCoO_2$ to be as low as 9.7 and 1.4 $W\,m^{-1}\,K^{-1}$ for in-plane and across-plane transport, respectively.[36] Their calculations were performed using the local-density approximation and include four-phonon scattering. Given the significantly higher cost of solid-state calculations with hybrid functionals over those with (semi-)local functionals such as LDA, it would be impractical to consider fourth-order interactions in the present study. In our previous work, we found that the LDA provided a good description of the phonon frequencies in $LiCoO_2$.[19] However, the LDA is generally insufficient for materials with strongly-correlated valence d electrons, and hybrid functionals such as HSE06 are in particular expected to be more robust in describing systems such as $LiNiO_2$ where unpaired electrons lead to Jahn-Teller distortions. Moreover, while fourth-order scattering may be required for $LiCoO_2$, the lower thermal conductivity of $LiNiO_2$ and $LiMnO_2$ mean that higher-order terms are unlikely to have as large a quantitative impact.

The frequency dependence of the modal group velocities, lifetimes and mean-free paths in the three $LiMO_2$ structures are compared in Figure 5. The group velocities of the modes

Table 2: Room-temperature (300 K) lattice thermal conductivities of $LiCoO_2$, $LiNiO_2$ and $LiMnO_2$ calculated with (Iso.) and without (No Iso.) scattering due to natural variation in atomic masses. Values are given in $W\,m^{-1}\,K^{-1}$.

	$LiCoO_2$		$LiNiO_2$		$LiMnO_2$	
	No Iso.	Iso.	No Iso.	Iso.	No Iso.	Iso.
xx	66.0	63.3	3.3	3.2	16.7	16.5
yy	66.0	63.3	9.4	9.2	4.6	4.5
zz	11.5	11.1	5.8	5.7	5.7	5.6
Ave.	47.8	45.9	6.2	6.0	9.0	8.9

that make the largest contributions to the thermal transport are on the same order of magnitude for all three oxides, ranging from 10^2 to 10^4 ms^{-1}, but the lifetimes display substantial variation, which results in $LiNiO_2$ and $LiMnO_2$ having 1–2 orders of magnitude shorter lifetimes and mean-free paths than $LiCoO_2$. The shorter lifetimes are evident across the entire frequency spectrum, indicating generally stronger phonon scattering in $LiNiO_2$ and $LiMnO_2$. By comparing the cumulative lattice thermal conductivity as a function of frequency at 300 K to the phonon DoS, we find that in all three compounds the low-frequency acoustic modes with large group velocity generally make the largest modal contributions to the heat transport (see Supporting Information). The suppressed lifetimes of these modes in $LiNiO_2$ and $LiMnO_2$ is therefore likely to be the biggest factor in the reduced thermal conductivity compared to $LiCoO_2$. The shorter lifetimes may be linked to the structural distortions, which would spread out the phonon frequencies and allow for a higher density of energy-conserving scattering events, thereby enhancing the phonon-phonon scattering and decreasing the lifetimes. The larger distortion in $LiMnO_2$ may be partially counteracted by the lighter mass of Mn, resulting in a slightly higher thermal conductivity than $LiNiO_2$ but a much lower one than the undistorted $LiCoO_2$.

The longer mean-free paths in $LiCoO_2$ may be suppressed in real electrode materials by boundary scattering due to small particle sizes. As shown in Figure 6, our calculations predict the averaged thermal conductivity to fall sharply as the grain size is reduced below ~ 1 μm, from 45.6 $W\,m^{-1}\,K^{-1}$ to 34.1, 12.7 and 2.29 $W\,m^{-1}\,K^{-1}$ when the mean-free paths

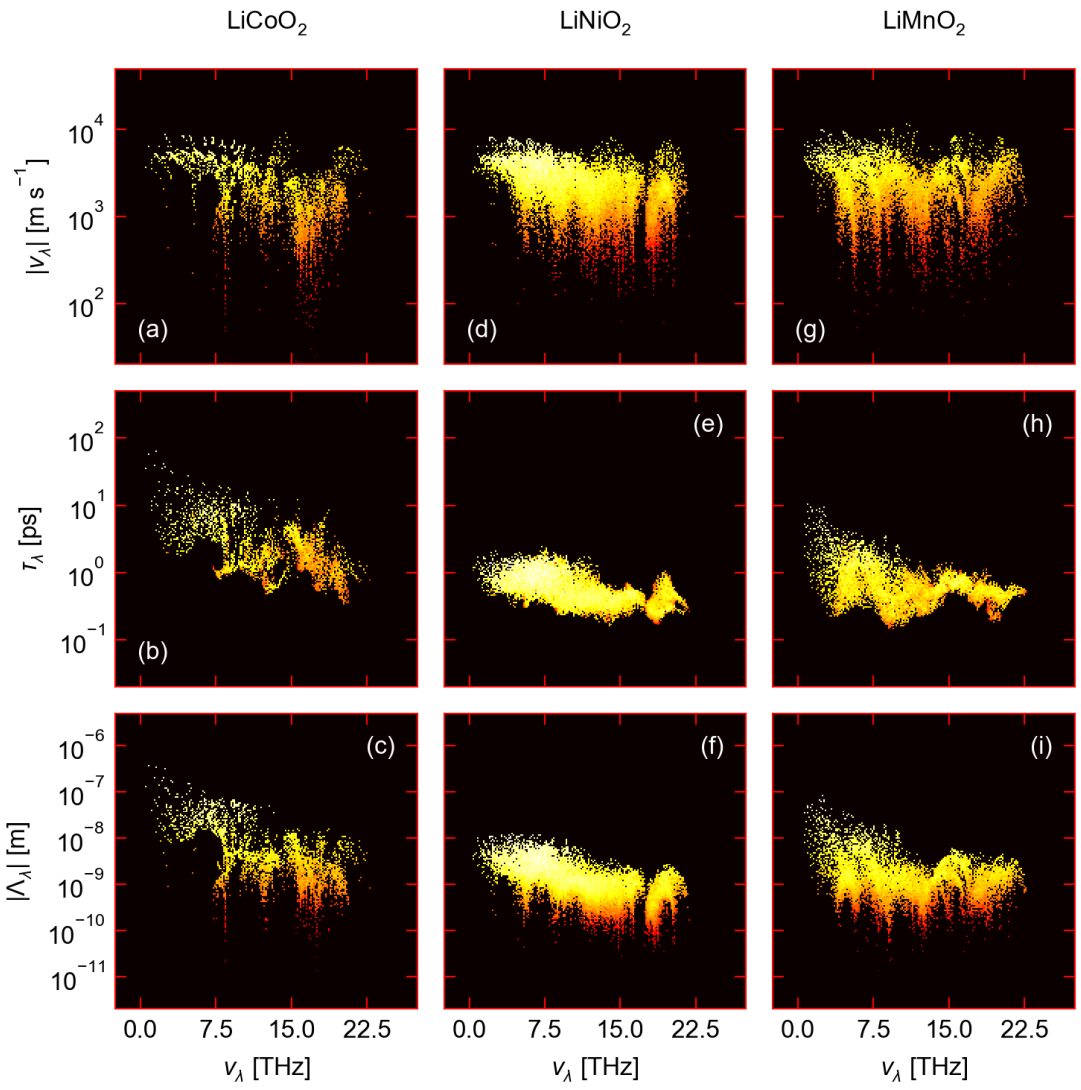

Figure 5: Breakdown of the thermal conductivity of (a-c) $LiCoO_2$ (left column), (d-f) $LiNiO_2$ (central column) and (g-i) $LiMnO_2$ (right column) at $T = 300$K. The top row (a, d, g) shows the spectrum of group velocities $|\nu_\lambda|$, the middle row (b, e, h) shows the modal lifetimes τ_λ, and the bottom row shows the mean-free paths $|\Lambda_\lambda|$ (c, f, i). The heat maps are colour coded by the average modal contributions to the thermal conductivity κ_λ along the three principal directions, from red (small κ) to yellow (large κ_λ).

are limited to 100, 10 and 1 nm, respectively. At the smaller sizes, we obtain results comparable to experimental measurements on $LiCoO_2$. The experimental thermal conductivities of polycrystalline $LiCoO_2$ was reported to be as low as 1.6–3.7 $W\,m^{-1}\,K^{-1}$,[18,37] which are reproduced with a limit of 1–2 nm in this work.

The shorter mean-free paths in $LiNiO_2$ and $LiMnO_2$ mean that the κ of these materials is suppressed less at smaller grain sizes, but nonetheless we observe a reduction from 5.94 and 8.09 $W\,m^{-1}\,K^{-1}$ at 100 nm to 4.65/5.26 $W\,m^{-1}\,K^{-1}$ at 10 nm and 1.73/1.71 $W\,m^{-1}\,K^{-1}$ at 1 nm. The implication of this result is that the thermal performance of $LiMO_2$ electrode materials may be highly sensitive to the preparation and processing, particularly for Co-rich compositions.

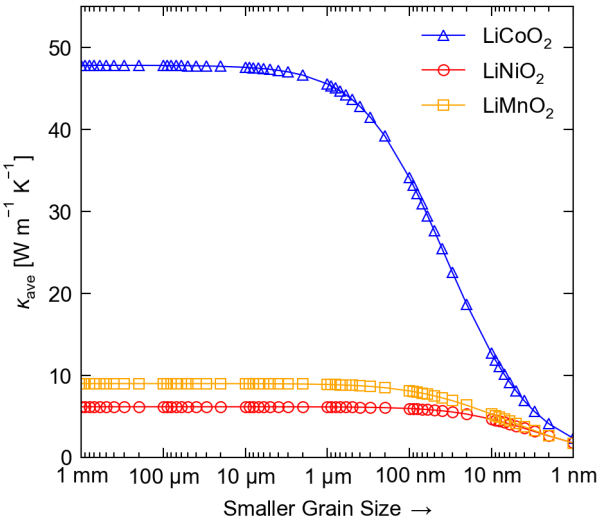

Figure 6: Effect of grain size on the average 300 K thermal conductivity $\kappa_{\text{ave}} = \frac{1}{3}(\kappa_{xx} + \kappa_{yy} + \kappa_{zz})$ of $LiCoO_2$ (blue triangles), $LiNiO_2$ (red circles) and $LiMnO_2$ (orange squares).

Transport in the NMC alloy

We consider two possibilities to describe the formation of NMC alloys: (1) a physical mixture of the three pure ternary oxides; and (2) a physical mixture of the crystal structures with proportional mixing at the transition metal sites.

In Case (1), the thermal conductivity of $Li(Ni_xMn_yCo_z)O_2$ ($x + y + z = 1$) is simply a linear combination of the three end members, i.e.:

$$\kappa[\mathrm{NMC}] = x \times \kappa_{\mathrm{LNO}} + y \times \kappa_{\mathrm{LMO}} + z \times \kappa_{\mathrm{LCO}} \tag{3}$$

where x, y, and z are molar fractions. κ_{LNO}, κ_{LMO} and κ_{LCO} are the thermal conductivities of $LiNiO_2$, $LiMnO_2$ and $LiCoO_2$, respectively. In the absence of experimental data to the contrary, a physical mixture of the pure endpoints is a reasonable possibility.

For Case (2), we make the assumption that the leading effects of the transition metal site disorder on the heat transport are due to the change in average mass and mass variance. A series of further thermal-conductivity calculations was performed on the three structures in which the average mass m_{ave} and mass variance m_{var} at the transition metal site was set to one of 66 compositions $Ni_xMn_yCo_z$ uniformly spaced on the ternary compositional diagram. The m_{ave} and m_{var} for each composition was calculated as:

$$m_{\mathrm{ave}} = \sum_i a_i \times m_i \tag{4}$$

$$m_{\mathrm{var}} = \sum_i a_i \times (1 - \frac{m_i}{m_{\mathrm{ave}}})^2 \tag{5}$$

where a_i and m_i are the fractions and masses of the three metals, i.e. $a_i = x, y, z$ and $m_i = m_{\mathrm{Ni}}, m_{\mathrm{Mn}}, m_{\mathrm{Co}}$. Ternary diagrams showing the modified thermal conductivity $\overline{\kappa}(x, y, z)$ for each of the three structures as a function of composition are shown in the Supporting Information.

The thermal conductivity of the mixture is then calculated as:

$$\overline{\kappa}[\mathrm{NMC}] = x \times \overline{\kappa}_{\mathrm{LNO}}(x, y, z) + y \times \overline{\kappa}_{\mathrm{LMO}}(x, y, z) + z \times \overline{\kappa}_{\mathrm{LCO}}(x, y, z) \tag{6}$$

This model is a variation on the mean-field approximation, which is a common method used

to model alloys. The change in the average mass at the transition metal site affects the phonon frequency spectrum and hence the heat capacities C_λ and group velocities ν_λ. The change in frequencies plus the change in average mass and mass variance also change the phonon scattering and hence the distribution of lifetimes τ_λ. This model does not however account for changes in the interatomic force constants due to the metal substitution, which, given the distinct JT distortions observed with Co, Ni and Mn, is likely to be a significant approximation.[38] However, to fully account for this would require a significant computational investment with a series of calculations on representative mixed-metal alloy structures, e.g. using the special quasi-random structure (SQS) method,[39,40] or by enumerating a full set of inequivalent structures in a representative supercell expansion.[41] We also note that, due to the substantial overhead of solving the full LBTE, the alloy calculations were performed using the RTA.

As shown in Table 2, the natural isotope effect reduces the average thermal conductivity of $LiCoO_2$, $LiNiO_2$ and $LiMnO_2$ by 4.3, 3.2 and 1.3 % at 300 K respectively. Calculations on $LiCoO_2$ with the mass of the transition metal varied between those of Co and Mn is predicted to have a non-linear impact on the room-temperature κ, with a substantial reduction from 45.9 to 39.3 $\mathrm{W\,m^{-1}\,K^{-1}}$ at 50 % Mn content and an increase in κ to 47.8 $\mathrm{W\,m^{-1}\,K^{-1}}$ at 100 % Mn content (Figure S4). Changing the mass from Co to Ni, on the other hand, leads to approximately linear variation in κ, which decreases from 45.9 $\mathrm{W\,m^{-1}\,K^{-1}}$ at 100 % Co content to 42.7 $\mathrm{W\,m^{-1}\,K^{-1}}$ at 100 % Ni content. While purely hypothetical, these examples show the two primary effects of varying the cation mass within a fixed structure type: reducing the average mass tends to increase κ, while larger mass variance tends to suppress heat transport. For this reason, within this model, mixing Mn and Co has a much larger impact on κ than mixing Co and Ni. These same effects are seen in the $LiNiO_2$ and $LiMnO_2$ structures, although they are less prominent due to the smaller κ of these structures (see Supporting Information). Nonetheless, mixing at the metal site is predicted to have a generally larger impact on κ than the natural isotope effect, even when assuming the leading

effect is simply the change in average mass and mass variance.

Table 3: Predicted thermal conductivity κ of three commercial NMC compositions at room temperature (300K) based on a physical mixture and a physical mixture with proportional mixing at the metal (M) site. Values are given in $\mathrm{W\,m^{-1}\,K^{-1}}$ and the % difference Δ between the two values is given in the fourth column.

$x:y:z$ in $Li(Ni_xMn_yCo_z)O_2$	Physical mixture	M-site Mixing	Δ [%]
111	20.2	17.9	-13.0
622	14.5	13.3	-9.4
811	10.3	9.7	-5.6

The predicted variation of κ for the NMC system is shown in Figure 7a assuming a physical mixture of the components, while Figure 7b shows the predicted reduction in κ if proportional mixing at the transition metal site is assumed to take place. Given the much higher thermal conductivity of $LiCoO_2$, both analyses predict the Co-rich compositions to have larger κ. Although $LiMnO_2$ is predicted to have a slightly higher κ than $LiNiO_2$, the proportional mixing model in Figure 7b suggests that mixing $LiMnO_2$ into Co-rich compositions will produce a larger suppression of κ due to the larger mass contrast.

We also consider three common commercial NMC compositions, *viz.* 811, 622 and 111, where the three numbers describe the ratios of Ni, Mn and Co (Table 3). Of these commercial compositions, NMC 811 has the lowest predicted thermal conductivity of 10.3 and 9.3 $\mathrm{W\,m^{-1}\,K^{-1}}$ based on the two models, while NMC 622 and NMC 111 are higher at 14.5/13.3 and 20.2/17.9 $\mathrm{W\,m^{-1}\,K^{-1}}$, respectively, due to the larger Co content. The suppression of κ due to proportional mixing at the metal site also increases in the order NMC 811 $<$ NMC 622 $<$ NMC 111, rising from 5.6 % in the former to 13 % in the latter.

Based on our modelling, we therefore conclude that site mixing in the alloys would have significant implications for heat transport. We note again that our models neglect microscopic effects due to mixing, which could further enhance the anharmonicity and lead to a further suppression of thermal conductivity. Ultimately, the question of whether these additional effects are important will most likely be determined by experimental measurements on the NMC system. The next challenge would be to describe interfacial thermal processes,

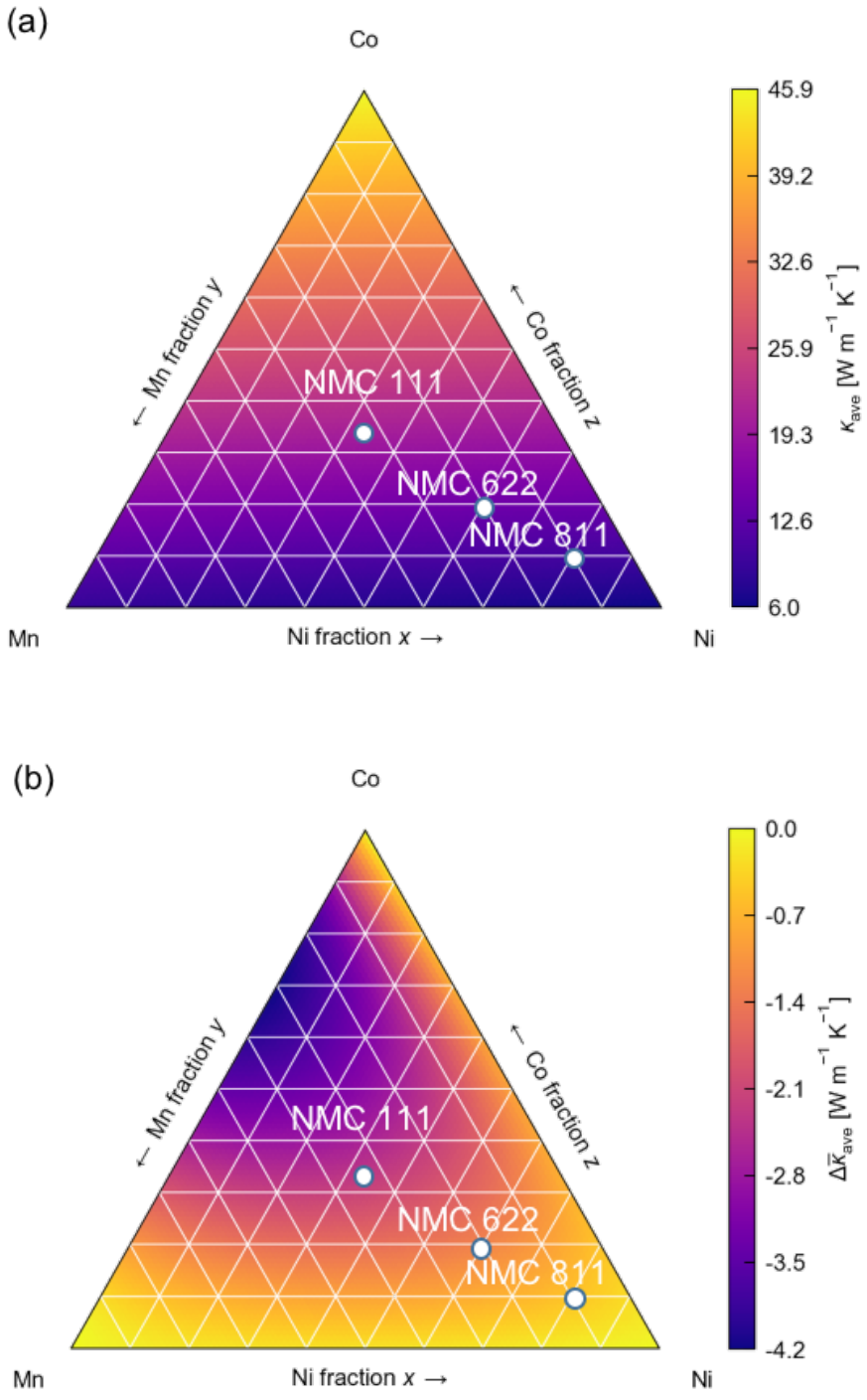

Figure 7: Ternary map of the thermal conductivity map κ of the NMC system. (a) is generated assuming a physical mixture of the pure components (Eqn. 3), while (b) shows the change in κ if proportional mixing at the transition metal site induces changes in the average mass and mass variation at the cation site (Eqn. 6).

in particular at the electrode/electrolyte junctions.[42–44]

Conclusion

In summary, we have carried out a detailed computational study of three lithium transition-metal oxides $LiCoO_2$, $LiNiO_2$ and $LiMnO_2$ and the commercial NMC alloy system. We elucidated how the different structural distortions impact the lattice dynamics and heat transport.

The three oxides show the same general structure type, but with Jahn-Teller distortions of the MO_6 octahedra depending on the transition metal oxidation states.[3,34] A strong preference for JT distortions in $LiMnO_2$ manifests itself as an imaginary harmonic mode at the M wavevector in the harmonic phonon dispersion calculated for the crystal structure obtained with XRD. Anharmonic phonon calculations show that while all three oxides have similar phonon group velocities, the distorted $LiNiO_2$ and $LiMnO_2$ structures have significantly shorter phonon lifetimes, which results in shorter mean-free paths and reduced thermal conductivity κ. We predict room-temperature values of 47.8, 8.9 and 6.2 $\mathrm{W\,m^{-1}\,K^{-1}}$ excluding isotope effects, which are likely to be upper limits, and are predicted to reduce significantly for small grain sizes.

We have also modelled the variation of the room-temperature thermal conductivity in the ternary NMC system based on a physical mixture of pure components and a physical mixture with proprtional mixing at the transition metal sites. The NMC 811, NMC 622 and NMC 111 compositions used in commercial electrodes have much smaller κ than $LiCoO_2$ due to the reduced Co content, and potential mass disorder due to mixing at the transition metal site is predicted to lead to significant further suppression of the heat transport. The thermal conductivity of the electrode materials is an important factor in the thermal management of batteries, and our results show that although the Ni/Mn-rich electrodes yield improved capacity and power performance this may need to be balanced against the effect on heat

transport. The insight from our first-principles studies should help in understanding the essential physical properties of the $LiMO_2$ systems. It will provide valuable information to guide experimental measurements and aid the design of future batteries with improved thermal management. Extensions of this work should consider the role of delithiation — following recent simulations that showed changes of up to 50–70%[36] — and dopants as additional avenues to influence the thermal transport in the NMC family.

Acknowledgement

We thank Jia-yue Yang for his contributions to the early stages of the project. This work was funded by the Faraday Institution (http://www.faraday.ac.uk, EP/S003053/1, grant no. FIRG003) and used the MICHAEL computing cluster. JMS is supported by a Presidential Fellowship from the University of Manchester. AW and BJM are supported by Royal Society University Research Fellowships (UF100278 and UF130329). *Via* our membership of the UK's HEC Materials Chemistry Consortium, which is funded by the EPSRC (EP/L000202, EP/R029431), this work used the ARCHER UK National Supercomputing Service (http://www.archer.ac.uk).

Supporting Information Available: (1) Convergence of the thermal conductivity κ of $LiCoO_2$, $LiNiO_2$ and $LiMnO_2$ with respect to the Brillouin-zone sampling mesh; (2) Effect of force-constant symmetrisation on κ; (3) Anisotropy in the thermal transport in the three materials; (4) Effect of grain size on the the heat transport along the three principal Cartesian directions; and (5) Affect of transition-metal mass variation in binary and ternary alloys based on the $LiCoO_2$, $LiNiO_2$ and $LiMnO_2$ structures.

References

(1) Ohzuku, T.; Makimura, Y. Layered lithium insertion material of $LiNi_{1/2}Mn_{1/2}O_2$: A possible alternative to $LiCoO_2$ for advanced lithium-ion batteries. *Chem. Lett.* **2001**, *30*, 744–745.

(2) Whittingham, M. S. Lithium batteries and cathode materials. *Chem. Rev.* **2004**, *104*, 4271–4302.

(3) Sun, H.; Zhao, K. Electronic Structure and Comparative Properties of $LiNi_xMn_yCo_zO_2$ Cathode Materials. *The J. Phys. Chem. C* **2017**, *121*, 6002–6010.

(4) Larcher, D.; Tarascon, J.-M. Towards greener and more sustainable batteries for electrical energy storage. *Nat. Chem.* **2015**, *7*, 19.

(5) Noh, H.-J.; Youn, S.; Yoon, C. S.; Sun, Y.-K. Comparison of the structural and electrochemical properties of layered $Li[Ni_xCo_yMn_z]O_2$ (x= 1/3, 0.5, 0.6, 0.7, 0.8 and 0.85) cathode material for lithium-ion batteries. *J. Power Sources* **2013**, *233*, 121–130.

(6) Dahn, J.; Von Sacken, U.; Juzkow, M.; Al-Janaby, H. Rechargeable $LiNiO_2$/carbon cells. *J. Electrochem. Soc.* **1991**, *138*, 2207–2211.

(7) Kim, M.-H.; Shin, H.-S.; Shin, D.; Sun, Y.-K. Synthesis and electrochemical properties of $Li[Ni_{0.8}Co_{0.1}Mn_{0.1}]O_2$ and $Li[Ni_{0.8}Co_{0.2}]O_2$ via co-precipitation. *J. Power Sources* **2006**, *159*, 1328–1333.

(8) Armstrong, A. R.; Bruce, P. G. Synthesis of layered $LiMnO_2$ as an electrode for rechargeable lithium batteries. *Nature* **1996**, *381*, 499.

(9) Goodenough, J. B.; Kim, Y. Challenges for Rechargeable Li Batteries. *Chem. Mater.* **2009**, *22*, 587–603.

(10) Tarascon, J.-M.; Armand, M. *Materials for Sustainable Energy*; World Scientific, 2011.

(11) Urban, A.; Seo, D.-H.; Ceder, G. Computational Understanding of Li-Ion Batteries. *npj Comput. Mater.* **2016**, *2*, 16002.

(12) Bandhauer, T. M.; Garimella, S.; Fuller, T. F. A critical review of thermal issues in lithium-ion batteries. *J. Electrochem. Soc.* **2011**, *158*, R1–R25.

(13) Zhao, Y.; Patel, Y.; Zhang, T.; Offer, G. J. Modeling the effects of thermal gradients induced by Tab and surface cooling on Lithium ion cell performance. *J. Electrochem. Soc.* **2018**, *165*, A3169–A3178.

(14) Zhao, Y.; Diaz, L. B.; Patel, Y.; Zhang, T.; Offer, G. J. How to Cool Lithium Ion Batteries: Optimising Cell Design using a Thermally Coupled Model. *J. Electrochem. Soc.* **2019**, *166*, A2849–A2859.

(15) Burheim, O. S.; Onsrud, M. A.; Pharoah, J. G.; Vullum-Bruer, F.; Vie, P. J. Thermal conductivity, heat sources and temperature profiles of Li-ion batteries. *ECS Trans.* **2014**, *58*, 145–171.

(16) Chen, S.-C.; Wang, Y.-Y.; Wan, C.-C. Thermal analysis of spirally wound lithium batteries. *J. Electrochem. Soc.* **2006**, *153*, A637–A648.

(17) Richter, F.; Vie, P. J.; Kjelstrup, S.; Burheim, O. S. Measurements of ageing and thermal conductivity in a secondary NMC-hard carbon Li-ion battery and the impact on internal temperature profiles. *Electrochim. Acta* **2017**, *250*, 228–237.

(18) Takahata, K.; Terasaki, I. Thermal conductivity of $AxBO_2$-type layered oxides $Na_{0.77}MnO_2$ and $LiCoO_2$. *Japanese J. Appl. Phys.* **2002**, *41*, 763.

(19) Yang, H.; Yang, J.-y.; Savory, C. N.; Skelton, J. M.; Morgan, B. J.; Scanlon, D. O.; Walsh, A. Highly Anisotropic Thermal Transport in LiCoO2. *The J. Phys. Chem. Lett.* **2019**, *10*, 5552–5556.

(20) Momma, K.; Izumi, F. VESTA 3 for three-dimensional visualization of crystal, volumetric and morphology data. *J. Appl. Crystallogr.* **2011**, *44*, 1272–1276.

(21) Hertz, J. T.; Huang, Q.; McQueen, T.; Klimczuk, T.; Bos, J.; Viciu, L.; Cava, R. J. Magnetism and structure of Li_xCoO_2 and comparison to Na_xCoO_2. *Phys. Rev. B* **2008**, *77*, 075119.

(22) Hirano, A.; Kanno, R.; Kawamoto, Y.; Takeda, Y.; Yamaura, K.; Takano, M.; Ohyama, K.; Ohashi, M.; Yamaguchi, Y. Relationship between non-stoichiometry and physical properties in $LiNiO_2$. *Solid State Ionics* **1995**, *78*, 123–131.

(23) Armstrong, A. R.; Bruce, P. G. Synthesis of layered $LiMnO_2$ as an electrode for rechargeable lithium batteries. *Nature* **1996**, *381*, 499–500.

(24) Kresse, G.; Furthmüller, J. Efficient iterative schemes for ab initio total-energy calculations using a plane-wave basis set. *Phys. Rev. B* **1996**, *54*, 11169.

(25) Kresse, G.; Furhmuller, J. Software VASP, Vienna (1999); PE Blöchl. *Phys. Rev. B* **1994**, *50*, 17953.

(26) Paier, J.; Marsman, M.; Hummer, K.; Kresse, G.; Gerber, I. C.; Ángyán, J. G. Screened hybrid density functionals applied to solids. *J. Chem. Phys.* **2006**, *124*, 154709.

(27) Tkatchenko, A.; DiStasio Jr, R. A.; Car, R.; Scheffler, M. Accurate and efficient method for many-body van der Waals interactions. *Phys. Rev. Lett.* **2012**, *108*, 236402.

(28) Bučko, T.; Lebègue, S.; Ángyán, J. G.; Hafner, J. Extending the Applicability of the Tkatchenko-Scheffler Dispersion Correction via Iterative Hirshfeld Partitioning. *J. Chem. Phys.* **2014**, *141*, 034114.

(29) Monkhorst, H. J.; Pack, J. D. Special points for Brillouin-zone integrations. *Phys. Rev. B* **1976**, *13*, 5188.

(30) Blöchl, P. E. Projector augmented-wave method. *Phys. Rev. B* **1994**, *50*, 17953.

(31) Togo, A.; Tanaka, I. First principles phonon calculations in Mater. Sci. *Scr. Mater.* **2015**, *108*, 1–5.

(32) Togo, A.; Chaput, L.; Tanaka, I. Distributions of phonon lifetimes in Brillouin zones. *Phys. Rev. B* **2015**, *91*, 094306.

(33) McGaughey, A. J.; Jain, A. Nanostructure Thermal Conductivity Prediction by Monte Carlo Sampling of Phonon Free Paths. *Appl. Phys. Lett.* **2012**, *100*, 061911.

(34) Du, T.; Xu, B.; Wu, M.; Liu, G.; Ouyang, C. Insight into the vibrational and thermodynamic properties of layered lithium transition-metal oxides $LiMO_2$ (M= Co, Ni, Mn): a first-principles study. *The J. Phys. Chem. C* **2016**, *120*, 5876–5882.

(35) Baur, W. The geometry of polyhedral distortions. Predictive relationships for the phosphate group. *Acta Cryst. B* **1974**, *30*, 1195–1215.

(36) Feng, T.; O'Hara, A.; Pantelides, S. T. Quantum prediction of ultra-low thermal conductivity in lithium intercalation materials. *Nano Energy* **2020**, 104916.

(37) Chen, S.; Wan, C.; Wang, Y. Thermal analysis of lithium-ion batteries. *J. Power Sources* **2005**, *140*, 111–124.

(38) Allan, N. L.; Stølen, S.; Mohn, C. E. Think locally–linking structure, thermodynamics and transport in grossly non-stoichiometric compounds and solid solutions. *J. Mater. Chem.* **2008**, *18*, 4124–4132.

(39) Zunger, A.; Wei, S.-H.; Ferreira, L.; Bernard, J. E. Special quasirandom structures. *Phys. Rev. Lett.* **1990**, *65*, 353.

(40) Grau-Crespo, R.; Hamad, S.; Catlow, C. R. A.; De Leeuw, N. Symmetry-adapted configurational modelling of fractional site occupancy in solids. *J. Phys.: Condens. Matter* **2007**, *19*, 256201.

(41) Gunn, D. S.; Skelton, J. M.; Burton, L. A.; Metz, S.; Parker, S. C. Thermodynamics, Electronic Structure, and Vibrational Properties of $Sn_n(S_{1-x}Se_x)_m$ Solid Solutions for Energy Applications. *Chem. Mater.* **2019**, *31*, 3672–3685.

(42) Haruyama, J.; Sodeyama, K.; Tateyama, Y. Cation mixing properties toward Co diffusion at the $LiCoO_2$ cathode/sulfide electrolyte interface in a solid-state battery. *ACS Appl. Mater. Int.* **2017**, *9*, 286–292.

(43) Benedek, P.; Yazdani, N.; Chen, H.; Wenzler, N.; Juranyi, F.; Månsson, M.; Islam, M. S.; Wood, V. C. Surface phonons of lithium ion battery active materials. *Sus. Energy & Fuels* **2019**, *3*, 508–513.

(44) Butler, K. T.; Gautam, G. S.; Canepa, P. Designing interfaces in energy materials applications with first-principles calculations. *npj Comp. Mater.* **2019**, *5*, 1–12.

Graphical TOC Entry